



# Phase transition sequences in tetramethylammonium tetrachlorometallates by X-ray diffraction and spectroscopic measurements

**HPSTAR**  
**457-2017**
**Jack Binns,<sup>a,b,\*</sup> Garry J McIntyre,<sup>b</sup> José A. Barreda-Argüeso,<sup>c</sup> Jesús González,<sup>c</sup> Fernando Aguado,<sup>c</sup> Fernando Rodríguez,<sup>c</sup> Rafael Valiente<sup>d</sup> and Simon Parsons<sup>a</sup>**

Received 14 February 2017

Accepted 28 April 2017

Edited by F. P. A. Fabbiani, Georg-August-Universität Göttingen, Germany

‡ Current affiliation: Center for High Pressure Science & Technology Advanced Research, 1690 Cailun Road, Pudong, Shanghai, 201203, People's Republic of China.

**Keywords:** phase transitions; crystal packing; intermolecular interactions.

**CCDC references:** 1546877; 1546878; 1546879; 1546880; 1546881; 1546882; 1546883; 1546884; 1546885; 1546886; 1546887; 1546888

**Supporting information:** this article has supporting information at journals.iucr.org/b

<sup>a</sup>EaStCHEM School of Chemistry and Centre for Science at Extreme Conditions, The University of Edinburgh, The King's Buildings, West Mains Road, Edinburgh EH9 3FJ, Scotland, <sup>b</sup>Australian Nuclear Science and Technology Organisation, New Illawarra Road, Lucas Heights, NSW 2234, Australia, <sup>c</sup>CITIMAC-Malta Team, Facultad de Ciencias, University of Cantabria, Santander, 39005, Spain, and <sup>d</sup>Dpto Física Aplicada, Facultad de Ciencias, University of Cantabria, Santander, 39005, Spain. \*Correspondence e-mail: jack.binns@hpstar.ac.cn

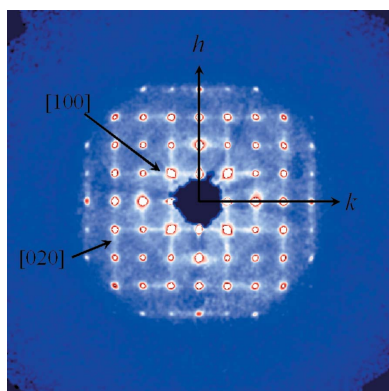
The phase transition sequences of two members of the tetramethylammonium tetrachlorometallate(III) family of hybrid organic–inorganic salts have been determined and structurally characterized as a function of temperature for the first time. Unusually, a reduction in point-group symmetry with increasing temperature until reaching a cubic prototype phase is observed. Two additional intermediate phases are observed for Fe<sup>3+</sup>. First-principles calculations and the presence of short Cl⋯Cl contacts for Ga<sup>3+</sup> suggest the [GaCl<sub>4</sub>]<sup>−</sup> anion to be conformationally hindered due to stronger lone-pair–σ-hole interactions. The conformationally more flexible Fe<sup>3+</sup> structures show sublattice melting with the onset of rotational disorder in the [NMe<sub>4</sub>]<sup>+</sup> cations occurring 40 K below the corresponding onset of rotational disorder in the [FeCl<sub>4</sub>]<sup>−</sup> sublattice.

## 1. Introduction

Despite their apparent simplicity, alkylammonium tetrahalometallates of *d*-block and other metals ([NR<sub>4</sub>]<sub>n</sub><sup>+</sup>[MX<sub>4</sub>]<sub>n</sub><sup>−</sup>, where *R* = H, Me, Et, *etc.*, *M* = Co<sup>2+</sup>, Fe<sup>2+</sup>, Zn<sup>2+</sup>, *etc.*, *X* = Cl, Br and *n* = 1 or 2) display a rich diversity of ferromagnetic, ferroelectric, ferroelastic and incommensurate phases within a relatively narrow range of thermodynamic conditions (López-Echarri *et al.*, 1990; Ruiz-Larrea *et al.*, 2000).

The earliest studies of these materials were primarily concerned with elucidating the geometries of tetrahedral metal ions such as [CuCl<sub>4</sub>]<sup>2−</sup> (Morosin & Lingafelter, 1959, 1961). Following the discovery of ferroelectricity in [NMe<sub>4</sub>]<sub>2</sub>ZnCl<sub>4</sub> by Sawada and colleagues, numerous experimental and theoretical studies of the bis-tetramethylammonium tetrahalometallates ([NMe<sub>4</sub>]<sub>2</sub>[MX<sub>4</sub>]) uncovered a complex but general phase diagram for *M* = Zn<sup>2+</sup>, Co<sup>2+</sup>, Fe<sup>2+</sup>, Mn<sup>2+</sup> and Cu<sup>2+</sup> (Sawada *et al.*, 1978; Shimizu *et al.*, 1980; Styczeń *et al.*, 2008; Zubillaga *et al.*, 1988; Clay *et al.*, 1975). These materials have become canonical models for studying disordered incommensurate–commensurate phase sequences (López-Echarri *et al.*, 1985). As for all materials in this class, the relationships between phases are governed by the orientations of component ions which reflect subtle changes in response to both temperature and pressure (Barreda-Argüeso *et al.*, 2014).

The range of structure types can be extended even further by selective or complete substitution of *R* groups. Recently, related hybrid organic–inorganic trihalide pseudo-perovskite materials such as methylammonium lead iodide (MeNH<sub>3</sub>PbI<sub>3</sub>)



have attracted significant attention as components of high-efficiency solar cells (Lee *et al.*, 2012). Substitution of the methyl groups for ethyl groups produces a new range of materials whose structures and phase sequences have only recently been fully characterized (Melia & Merrifield, 1971; Wolhuis *et al.*, 1986; Mahoui *et al.*, 1996; Kandhaswamy & Srinivasan, 2002; Wyrzykowski, Kruszyński *et al.*, 2008; Lutz *et al.*, 2014).

The subset of alkylammonium tetrahalometallates with  $R = \text{Me}$ , and  $n = 1$ , has not been subject to the same level of systematic investigation as the  $n = 2$  materials. Góśniowska and colleagues report calorimetric data which suggest three first-order transitions for tetramethylammonium tetrabromindate(III),  $[\text{NMe}_4][\text{InBr}_4]$ , although structures of the transformed phases were not reported (Góśniowska *et al.*, 2000). NMR data indicate that tetramethylammonium tetrachlorothallate(III) undergoes a single phase transition at 239 K (Lenck *et al.*, 1991).

Tetramethylammonium tetrachloroferrate(III),  $[\text{NMe}_4][\text{FeCl}_4]$ , (TCF), has attracted attention for the numerous phase transitions reported in the relatively narrow range of temperatures from 220 to 400 K. Czaplá *et al.* report phase transitions (upon heating) at 291, 303, 314, 322, 347 and 384 K detected by differential scanning calorimetry (DSC) measurements (Czaplá *et al.*, 1985). Above 520 K the material decomposes. Subsequently Ruiz-Larrea *et al.* carried out adiabatic calorimetry and DSC measurements and report phase transitions (upon heating) at 236.1, 291.4, 307.4, 347.0 and 381.0 K (Ruiz-Larrea *et al.*, 1987). Optical microscopy and linear birefringence measurements by Kosturek *et al.* confirm the presence of four first-order transitions at 385, 303, 294 and 265 K on cooling (Kosturek *et al.*, 1999). Kosturek *et al.* note that transitions in this material are subject to very large thermal hystereses and the exact critical temperature of a transition is very much dependent upon the thermal history of the sample.

The only crystal structure in the series reported to date is the phase at room temperature, which is orthorhombic with  $a = 14.2746$  (12),  $b = 6.4431$  (5), and  $c = 6.4401$  (5) Å (Wyrzykowski, Kruszyński *et al.*, 2008). The space group was initially reported to be  $Pmc2_1$  ( $P2_1am$  using the above unit-cell dimensions; Czaplá *et al.*, 1985), but this was later revised to  $Pma2$  (Wyrzykowski, Kruszyński *et al.*, 2008).

We now report crystallographic, calorimetric and spectroscopic data for phases obtained between 100 and *ca* 400 K for TCF and tetramethylammonium tetrachlorogallate(III),  $[\text{NMe}_4][\text{GaCl}_4]$ , (TCG), a previously unreported analogue of TCF, complemented with calorimetric measurements. Unusually, the symmetries of both materials decrease on heating until high-symmetry plastic phases form in a narrow range at high-temperature prior to amorphization. In TCF, symmetry reduction occurs *via* a sequence of phases which show a step-wise loss of orientational correlation. TCG shows fewer intermediate steps; correlation is lost entirely in one step before the onset of full rotational disorder. Raman and UV–vis–NIR spectroscopy indicate phase transitions in excellent agreement with crystallographic results. The

temperature dependence of internal ionic modes provides quantitative agreement between vibrational and crystal-structure thermal dependences.

## 2. Methods

### 2.1. Calorimetric and spectroscopic measurements

Differential scanning calorimetry (DSC) was carried out over the temperature range 93 to 400 K at a scan rate of  $150 \text{ K h}^{-1}$  at the Thermal Analysis Facility at the University of Durham, UK. Single-crystal samples were cooled to 105 K before undergoing a cycle of heating and cooling between a maximum of 402 K and a minimum of 105 K.

Unpolarized Raman spectra were obtained using the 514.5 and 647 nm lines of an  $\text{Ar}^+ - \text{Kr}^+$  laser with a Horiba T64000 spectrometer equipped with a nitrogen-cooled CCD and a confocal microscope for detection. Temperature measurements in the 290–450 K range were accomplished with a heating stage (Linkam TS-1000) equipped with a temperature controller.

UV–vis–NIR absorption spectra in the range 200–1800 nm were measured with a Cary 6000i spectrometer (Varian). Multidomain single crystals of parallelepipedic shape were selected from the mother liquor for variable-temperature optical transmission measurements. A closed-cycle cryostat (ARS) and a heating stage (Leitz 350) were used for temperature-dependent studies. Temperature ramps were fixed at  $120 \text{ K h}^{-1}$ . The temperature dependence of the absorbance at a fixed wavelength (582 nm for TCF and 660 nm for TCG) was used to characterize the phase transitions through changes of the refractive index ellipsoid. Data were collected as follows: an as-grown multidomain single-crystal was first cooled down from room temperature to 200 K and then heated from 200 K to room temperature. Because the results depend on the thermal history of the sample, another crystal was then selected and heated up from room temperature to *ca* 400 K, and then cooled down to room temperature. This procedure was carried out for both TCF and TCG.

### 2.2. Crystallization and single-crystal X-ray diffraction

Single crystals of  $[\text{NMe}_4][\text{FeCl}_4]$  (TCF) and  $[\text{NMe}_4][\text{GaCl}_4]$  (TCG) were grown over the course of several weeks by slow evaporation at 303 K of aqueous solutions containing  $\text{NMe}_4\text{Cl}$  and  $\text{FeCl}_3 \cdot 6\text{H}_2\text{O}$  or  $\text{GaCl}_3 \cdot 6\text{H}_2\text{O}$  in a 1:1 stoichiometric ratio. The samples contained crystals of up to  $1 \text{ mm}^3$ , and suitably sized crystals were selected for different experiments.

Single-crystal diffraction data were collected on an Agilent Supernova using a  $\text{Mo K}\alpha$  microsource ( $\lambda = 0.71073 \text{ \AA}$ ) equipped with an Oxford Cryosystems variable-temperature device. Data were integrated using *CrysAlisPro*, absorption corrections were carried out in *ABSPACK* (Agilent, 2014).

Single-crystal X-ray diffraction data were collected at 180, 300 and 393 K to identify the three TCG phases. For TCF the variable-temperature single-crystal diffraction data-collection strategy followed the phase sequence from 220 to 385 K on freshly prepared samples cooled from room temperature;

fresh samples were used to avoid the significant hysteresis observed for phase transitions in these materials.

### 2.3. Refinement and twinning

Although the phase sequences of TCF and TCG are similar, not all the phases seen for TCF are seen for TCG. To avoid labelling phases out of sequence or with absent members, phases are labelled using their Pearson symbols which identify similar phases in the respective sequences. The two letters specify the Bravais lattice used followed by the number of atoms in the unit cell.

Structures were solved in *SIR92* (Altomare *et al.*, 1993) or *SUPERFLIP* (Palatinus & Chapuis, 2007), refinements were carried out against  $|F|^2$  in *CRYSTALS* (Betteridge *et al.*, 2003) or *SHELXL* (Sheldrick, 2015). Rigid-body and rigid-bond restraints were applied to the displacement parameters of the  $[\text{NMe}_4]^+$  cation for TCF-*mP22*, TCG-*mP22*, and TCF-*oP44*. The refinement of phases TCF-*mP22* and TCG-*mP22* also required the use of bond-angle and bond-distance restraints for the  $[\text{NMe}_4]^+$  cation; these restraints are validated by Raman spectroscopy, which shows that both ions remain tetrahedral over the temperature ranges studied (§3.2). The structures of phases TCF-*mP44*, TCF-*cP22*, and TCG-*cP22* contain rotationally disordered  $[\text{NMe}_4]^+$  cations, which were modelled using the spherical-shell shape implemented in *CRYSTALS* (Schröder *et al.*, 2004). The carbon-shell model has six potentially refinable parameters. The occupancy was fixed at four C atoms and the coordinates of the centre of the sphere were fixed by symmetry. The radius and isotropic displacement factor were allowed to vary.

Although most crystals of TCF suffered from twinning, a sample was eventually found which consisted of one domain in the TCF-*oP88* and TCF-*oP44* phases. This sample was used in the data collections of phases TCF-*oP88*, TCF-*oP44* and TCF-*mP22*. A second crystal was used for the structure determination of TCF-*mP44* owing to degradation of the sample. Twinning was handled during data reduction with multiple orientation matrices applied in the integration program *CrysAlisPro*. Data were also integrated with a single orientation matrix with twinning treated in the refinement. However treating the data as twinned during integration provided the best refinement statistics.

The diffraction patterns of TCF-*mP22* and TCG-*mP22* could both be indexed using orthorhombic *C*-centred cells, with apparent space group *Cmmm*. Unit-cell dimensions for TCF were  $a = 8.974$  (2),  $b = 9.204$  (2) and  $c = 7.1747$  (12) Å; those for TCG were  $a = 9.027$  (11),  $b = 9.235$  (13) and  $c = 7.1473$  (9) Å. Solutions of these structures yielded highly disordered models exhibiting poor fits to the data. However, splitting peaks at high angle suggested that the symmetry was in fact monoclinic. Re-indexing revealed two metrically pseudo-tetragonal monoclinic domains indicating that the crystal was a pseudomerohedral twin.

The unit-cell dimensions of TCF-*mP22* were  $a = 6.425$  (3),  $b = 7.1480$  (16) and  $c = 6.4274$  (18) Å,  $\beta = 91.21$  (3)°. A total of 3580 reflections were indexed; 1046 were assigned to domain 1

only, 899 to domain 2 with the remainder overlapped, a total of 279 reflections were unindexed. The relationship between the orientation matrices of the two indexed domains was a rotation of 90° about the *b*-axis, expressed by the twin law<sup>1</sup>

$$\begin{pmatrix} 0 & 0 & \bar{1} \\ 0 & 1 & 0 \\ 1 & 0 & 0 \end{pmatrix}$$

The structure of TCF-*mP22* was solved and modelled in space group *Pm*. Analysis of this structure, and also that of TCG-*mP22*, was attempted in space groups *P2*, *P2/m*, *Pm*. Only the refinements in *Pm* gave reasonable bond lengths and acceptable *R*-factors. Coset decomposition of point group *4/mmm* with respect to point group *2/m* gives a total of four possible domains and in addition to the fourfold rotation around the *b*-axis identified during indexing, two further twin laws, a twofold rotation around the *a*-axis and a twofold rotation about the *ac* face-diagonal, were applied during the refinement (Flack, 1987; Schlessman & Litvin, 1995). Refined twin scale factors were 0.393 (12), 0.358 (13), 0.155 (11) and 0.094 (4). This twinning model neglects the absolute structure of the four domains, which would require the addition of a further four twin laws given by the decomposition of *4/mmm* into *m* (these laws are obtained by the addition of an inversion operator to each of the four domains in the model). Attempts to include these twin laws into the model led to refinement instabilities.

Data were collected on a crystal of TCG-*mP22* selected directly from the mother liquor. Again two monoclinic domains could be identified, related by a 90° rotation about the *b*-axis, with unit-cell dimensions  $a = 6.4478$  (14),  $b = 7.1316$  (7), and  $c = 6.4451$  (8) Å,  $\beta = 91.399$  (14)°. Of the 4615 reflections used for indexing, 2204 were assigned to domain 1, 723 to domain 2 only, with 1656 overlapped reflections; the remaining 32 reflections could not be assigned to either domain. Refinement was carried out using a two-domain model with the fourfold rotation given above; the additional twin laws ( $2_{[100]}$ ) and ( $2_{[101]}$ ) yielded no improvement to the data fitting. The final twin scale factor was 0.463 (7). The twinning was confirmed to persist in TCG-*oP88* obtained when the same sample was cooled. Data from one of the domains were integrated and used for refinement.

### 2.4. Powder diffraction measurements

Variable-temperature X-ray powder diffraction data were collected on samples of TCF and TCG using a Bruker D8 ADVANCE diffractometer equipped with a Lynxeye position-sensitive detector and an Oxford Cryosystems low-temperature device. The radiation source was Ge-monochromated Cu  $K\alpha_1$ . The temperature stability of the variable-temperature device was  $\pm 0.1$  K over the temperature range 120–400 K. For the 5 and 10 K steps a ramp rate of 10 K h<sup>-1</sup> was used; this was increased to 360 K h<sup>-1</sup> for larger steps. The temperature was equilibrated for at least 30 min before

<sup>1</sup> Twin laws refer to reciprocal space directions (*hkl*) expressed as column vectors.

**Table 1**

Phase transitions, critical temperatures and enthalpy changes.

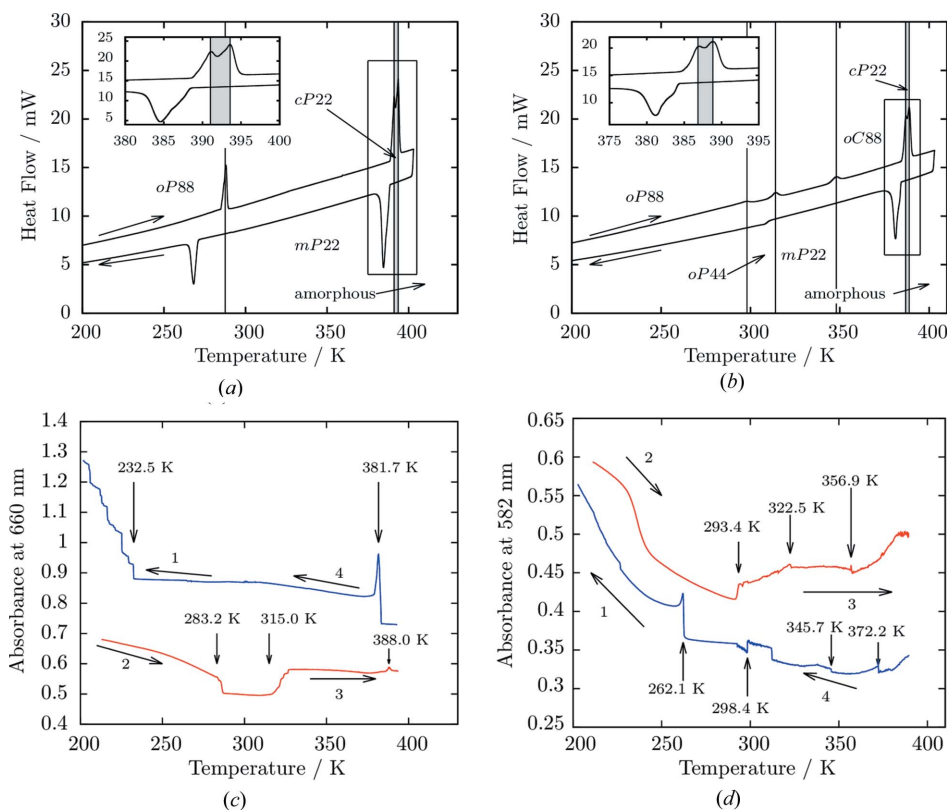
Figures marked in bold correspond to the sum of two transitions.

Transitions (TCF)	$T_C$ (DSC) (K)	$\dagger T_C$ (K)	$\ddagger T_C$ (K)	$T_C$ (OM) (K)	$\Delta H$ (DSC) (kJ mol <sup>-1</sup> )
<i>oP88</i> → <i>oP44</i>	288.2	288	291	293.4	0.4089
<i>oP44</i> → <i>mP22</i>	310.9	307	307	311.0	0.6016
<i>mP22</i> → <i>mP44</i>	344.4	341	347	345.7	0.6183
<i>mP44</i> → <i>cP22</i>	386.84	386	381	372.2	<b>6.0791</b>
<i>cP22</i> → amorphous	388.84			–	

Transitions (TCG)	$T_C$ (DSC) (K)	$T_C$ (OM) (K)	$\Delta H$ (DSC) (kJ mol <sup>-1</sup> )
<i>oP88</i> → <i>mP22</i>	286.15	283.2	2.3455
<i>mP22</i> → <i>cP22</i>	391.04	388.0	<b>6.3893</b>
<i>cP22</i> → amorphous	393.58	–	

 † Kosturek *et al.* (1999). ‡ Ruiz-Larrea *et al.* (1987).

collections. Unit-cell dimensions were determined by Le Bail fitting carried out in *JANA2006* (Petříček *et al.*, 2014) and fitted to a Berman thermal equation-of-state in *EOSFIT 7.0* to determine thermal expansivities (Berman, 1988; Angel *et al.*, 2014).


**Figure 1**

DSC data showing heat flow per gram of sample for TCG (a), three phase transitions are apparent on heating at 286.15, 391.04 and 393.58 K; (b) DSC data for a single crystal of TCF. The five phase transitions upon heating are marked with vertical lines. Insets display the two transitions in the region of the high-temperature *cP22* phase (shaded). Thermal evolution of the sample optical absorbance at 660 and 582 nm for TCG (c) and TCF (d), respectively. The thermal sequence is labelled with numbers (see text); red curves corresponding to heating runs and blue curves correspond to cooling runs.

**Table 2**

 Symmetry and frequency ( $\nu_i$ ) of the Raman active modes of TCF and TCG single crystals at room temperature.

 Peak frequencies correspond to internal modes of  $[MCl_4]^-$  tetrahedra.

Raman shift	Bending modes Cl–M–Cl	Stretching modes M–Cl		
$\nu$ (cm <sup>-1</sup> )	$\nu_2$ (E)	$\nu_4$ (T <sub>2</sub> )	$\nu_1$ (A <sub>1</sub> )	$\nu_3$ (T <sub>2</sub> )
$[\text{GaCl}_4]^-$	116.4	148.1	346.8	374.5
$[\text{FeCl}_4]^-$	112.2	136.3	335.0	371.5
$[\text{FeCl}_4]^\dagger$	114	136	330	378

† Nakamoto (2006).

## 2.5. DFT calculations

Geometry-optimization calculations were carried out using the plane-wave density-functional theory computational package *CASTEP6.11* (Clark *et al.*, 2005). The generalized gradient approximation as expressed in the Perdew–Burke–Ernzerhof (PBE) exchange–correlation functional was used with ‘on-the-fly’ pseudopotentials generated by *CASTEP*, and the application of the TS semi-empirical dispersion correction scheme (Perdew *et al.*, 1996; Tkatchenko & Scheffler, 2009). Basis-set kinetic energy cut-offs and Monkhorst–Pack grid

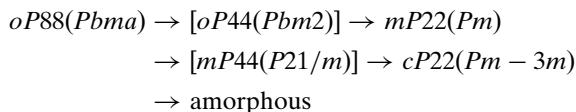
densities were chosen to converge total energy differences of  $dE_{\text{tot}}/dE_{\text{cut}} < 0.001$  eV atom<sup>-1</sup>, giving values of  $E_{\text{cut}} = 500$  eV for both TCF and TCG and a Monkhorst–Pack  $k$ -point grid of  $3 \times 3 \times 4$ . Convergence criteria for the geometry optimizations were: maximum change in total energy of  $2.0 \times 10^{-5}$  eV atom<sup>-1</sup>, maximum force 0.05 eV Å<sup>-1</sup>, maximum root-mean-square atomic displacement of 0.002 Å, and maximum stress 0.1 GPa. Experimentally derived structures provided starting coordinates for the geometry optimizations, which optimized unit-cell dimensions and atomic coordinates.

## 3. Results and analysis

### 3.1. Phase transition sequences

X-ray crystallography, differential scanning calorimetry and optical absorbance measurements identified a total of three phase transitions in TCG and five phase transitions in TCF. All structures, with the exception of the ambient-pressure phase of TCF (TCF-*oP44*), are previously unreported. Of the five TCF phases, three were structurally closely related to, but not

precisely isostructural with the equivalent TCG phases, so the phase sequence of TCF can be considered to be analogous to TCG with two additional intermediate phases. The general phase sequence found in these compounds on heating is given below; the phases observed in TCF but not TCG are shown in square brackets.



DSC and optical absorbance measurements for TCG (Fig. 1a) show the presence of three first-order transitions peaking at 286.15, 391.04 and 393.58 K. Data for TCF (Fig. 1a) indicate a total of five transitions on heating a freshly prepared sample between 100 and 400 K. This is in agreement with Kosturek *et al.* (1999) for a sample cooled from room temperature to 220 K and then heated to 390 K. The critical temperatures for phase transitions in both materials are given in Table 1 along with literature values and enthalpy changes.

UV-vis-NIR absorption is a powerful procedure for detecting phase transitions in optically transparent samples because of changes in the refractive index ellipsoid which yields discontinuities in the absorbance *versus* temperature  $A(T)$  curve. This method is also suitable for determining thermal hysteresis, detecting domain formation and in determining how a phase transition propagates in different domains, giving rise to ladder-like  $A(T)$  variations due to shifts of critical temperature in each domain due to sample thermal history (Valiente & Rodríguez, 1998). There is close agreement between the critical temperatures derived from DSC and optical measurements (OM), however the OM data clearly shows discontinuities corresponding to all transitions on cooling as well as during heating which are absent in DSC (Table 1). Conversely, DSC is able to clearly distinguish the narrow stability range of the  $cP22$  phases illustrating the value

in performing both sets of measurements for determining the presence of phase transitions in a material.

The narrow stability range of the  $cP22$  phases on heating (TCG: 2.54 K; TCF: 2.00 K) in both materials results in overlapping peaks in the DSC data between the  $mP44 \rightarrow cP22$  and  $cP22 \rightarrow$  amorphous transitions [*cf.* Fig. 1(a) and 1(b) insets]. Variable-temperature powder diffraction for TCF shows the presence of a cubic phase stable in the narrow range 386–389 K before the sample becomes amorphous. Shoulders are also visible on the corresponding DSC peaks upon cooling, although they are less well defined for both materials. It is also noteworthy that there is no peak upon cooling, corresponding to the  $mP22 \rightarrow mP44$  transition for TCF.

### 3.2. Raman spectroscopy

Fig. 2 shows the unpolarized Raman spectra of TCF and TCG at room temperature. The spectra consist of three groups of peaks. The first low-energy group at *ca* 100  $\text{cm}^{-1}$  corresponds to bending modes of the anions ( $E + T_2$ ). The second group located around 300  $\text{cm}^{-1}$  is ascribed to stretching modes ( $T_2 + A_1$ ) of the  $[\text{GaCl}_4]^-$  and  $[\text{FeCl}_4]^-$  units. The third group related to the high-frequency peak at 750  $\text{cm}^{-1}$  corresponds to the stretching mode ( $A_1$ ) of the N–CH<sub>3</sub> bonds of the cation. Although the Raman peaks were partially known for  $[\text{FeCl}_4]^-$  in solution and other compounds (Nakamoto, 2006), here we report a full characterization of the Raman modes in TCF and TCG, constituting the first study of the vibrational modes for both  $[\text{GaCl}_4]^-$  and  $[\text{FeCl}_4]^-$  anions in the solid state. Peak frequencies and mode assignment are summarized in Table 2.

The frequency of the totally symmetric anion stretching mode ( $A_1$ ) is higher for the TCG than for TCF as expected for the different average  $M-L$  distances  $d(\text{Ga}-\text{Cl}) = 2.170 \text{ \AA}$  (Jakubas *et al.*, 1997) and  $d(\text{Fe}-\text{Cl}) = 2.177 \text{ \AA}$  (Wyrzykowski, Kruszyński *et al.*, 2008) both at 291 K. The corresponding frequency of the stretching mode  $A_1$  of the cation ( $\nu_1 = 750 \text{ cm}^{-1}$ ) is the same for TCF and TCG, indicating that all these crystal modes mainly correspond to internal vibrations of the molecular ions behaving as independent tetrahedral subunits. The  $A_1$  and  $E$  frequencies depend on both the  $M-L$  force constant and the  $\text{Cl}^-$  mass but are independent of the  $M$  mass, whereas  $T_2$  modes depend on the reduced mass involving both  $\text{Cl}^-$  and  $M$ . For a given force constant, their relative frequency reduces on replacing Fe for Ga but this shift is very small ( $< 1\%$ ) due to the similar masses of Ga (69.72) and Fe (55.85). The fact that Raman spectra are similar for TCF and TCG single crystals and do not show any additional peaks or splitting of the  $T_2$ -mode peaks as

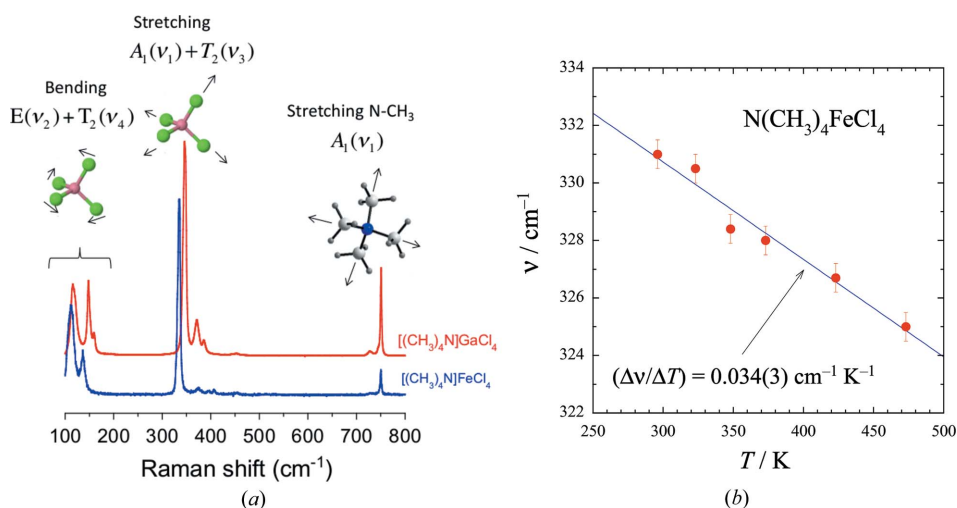


**Figure 2**  
Unpolarized single-crystal Raman spectra of  $[(\text{CH}_3)_4\text{N}]\text{FeCl}_4$  (TCF) and  $[(\text{CH}_3)_4\text{N}]\text{GaCl}_4$  (TCG) at room temperature with peak assignment.

**Table 3**  
Crystallographic information for TCF phase sequence.

Chemical formula for TCF is  $C_4H_{12}N \cdot FeCl_4$ ,  $M_r = 271.80$ . Mo  $K\alpha$  radiation.

	TCF- <i>oP88</i>	TCF- <i>oP44</i>	TCF- <i>mP22</i>	TCF- <i>mP44</i>	TCF- <i>cP22</i>
<b>Crystal data</b>					
Crystal system, space group	Orthorhombic, <i>Pbcm</i> ( <i>bca</i> ) (No. 57)	Orthorhombic, <i>Pma2</i> ( <i>ba\bar{c}</i> ) (No. 28)	Monoclinic, <i>Pm</i> (No. 6)	Monoclinic, <i>P2<sub>1</sub>/m</i> (No. 11)	Cubic, <i>Pm\bar{3}m</i> (No. 221)
Temperature (K)	220	295	318	365	385
<i>a</i> , <i>b</i> , <i>c</i> (Å)	13.1442 (8), 13.9946 (8), 6.4272 (3)	6.4471 (5), 14.2753 (11), 6.4526 (5)	6.425 (3), 7.1480 (16), 6.4274 (18)	6.574 (3), 14.156 (7), 6.595 (3)	6.8470 (5), 6.8470 (5), 6.8470 (5)
$\beta$ (°)	90	90	91.21 (3)	93.87 (4)	90
<i>V</i> (Å <sup>3</sup> )	1182.27 (11)	593.86 (8)	295.12 (17)	612.3 (5)	321.00 (7)
Twin obliquity (°)	0.0	0.05	1.20	0.184	0.0
<i>Z</i>	4	2	1	2	1
<i>F</i> (000)	548	274	125	202	202
$\mu$ (mm <sup>-1</sup> )	2.12	2.11	2.13	2.05	1.95
Crystal size (mm)	0.05 × 0.08 × 0.10	0.05 × 0.08 × 0.10	0.05 × 0.08 × 0.10	0.05 × 0.05 × 0.10	0.05 × 0.05 × 0.10
<b>Data collection</b>					
Absorption correction	Multi-scan <i>CrysAlis</i>	Multi-scan <i>CrysAlis</i>	Multi-scan <i>CrysAlis</i>	Multi-scan <i>CrysAlis</i>	–
<i>T</i> <sub>min</sub> , <i>T</i> <sub>max</sub>	0.84, 0.90	0.73, 0.90	0.60, 0.90	0.49, 0.90	–
$\theta$ <sub>min</sub> , $\theta$ <sub>max</sub> (°)	3.1, 25.7	3.2, 26.4	3.2, 25.5	3.1, 20.9	3.0, 13.4
No. of measured, independent and observed [ <i>I</i> > 2σ( <i>I</i> )] reflections	17 459, 1169, 1007	1248, 1248, 1160	1184, 1184, 1040	5173, 675, 576	1895, 21, 18
Unmerged total reflections	19 658	10 703	5211	12 844	9899
<i>R</i> <sub>int</sub>	0.043	0.042	0.133	0.065	0.059
Range of <i>h</i> , <i>k</i> , <i>l</i>	<i>h</i> = 0 → 16, <i>k</i> = 0 → 16, <i>l</i> = 0 → 7	<i>h</i> = 0 → 8, <i>k</i> = 0 → 17, <i>l</i> = -8 → 8	<i>h</i> = -7 → 7, <i>k</i> = 0 → 8, <i>l</i> = -7 → 7	<i>h</i> = -6 → 6, <i>k</i> = 0 → 14, <i>l</i> = 0 → 6	<i>h</i> = 0 → 2, <i>k</i> = 0 → 3, <i>l</i> = 1 → 4
Range of unmerged <i>h</i> , <i>k</i> , <i>l</i>	<i>h</i> = -17 → 17, <i>k</i> = -16 → 16, <i>l</i> = -8 → 8	<i>h</i> = -8 → 8, <i>k</i> = -19 → 19, <i>l</i> = -8 → 8	<i>h</i> = -8 → 8, <i>k</i> = -8 → 8, <i>l</i> = -8 → 8	<i>h</i> = -9 → 9, <i>k</i> = -21 → 21, <i>l</i> = -9 → 9	<i>h</i> = -9 → 9, <i>k</i> = -9 → 9, <i>l</i> = -9 → 8
<b>Refinement</b>					
<i>R</i> [ <i>F</i> <sup>2</sup> > 2σ( <i>F</i> <sup>2</sup> )], <i>wR</i> 2, <i>S</i>	0.0391, 0.0740, 1.00	0.0581, 0.1301, 0.96	0.0711, 0.1864, 0.94	0.1190, 0.2057, 1.04	0.0981, 0.1380, 0.99
No. of reflections	1162	1243	1182	665	18
No. of parameters	51	52	58	32	14
$\Delta\rho$ <sub>max</sub> , $\Delta\rho$ <sub>min</sub> (e Å <sup>-3</sup> )	0.41, -0.50	1.14, -0.78	0.82, -0.68	0.59, -0.62	0.18, -0.25

temperature increases allows us to conclude that the cations and anions preserve their tetrahedral local symmetry, justifying the use of bond-angle and bond-distance restraints in the X-ray refinements of [NMe<sub>4</sub>]<sup>+</sup> cations. Vibrational spectroscopy is a very sensitive probe of changes in primary bonds and the absence of any significant changes in frequency with temperature, beyond a linear softening, confirms that the phase transitions are intermolecular in nature, and not a result of electronic effects in the constituent ions.

The shift in the anionic *A*<sub>1</sub> stretching-mode frequency in going from [FeCl<sub>4</sub>]<sup>-</sup> to [GaCl<sub>4</sub>]<sup>-</sup> is 11.8 cm<sup>-1</sup>; the corresponding value for the *T*<sub>2</sub> mode is much smaller at 3 cm<sup>-1</sup>. The former depends on the *M*–*L* force constant which is expected to increase by about 4% for Ga–Cl if it is assumed that the *M*–*L* distance, *d*, dependence of force constant is *d*<sup>-3γ</sup> with γ = 1.4 (Barreda-Argüeso *et al.*, 2014) taking average *M*–Cl distances of *d*(Fe–Cl) = 2.186 Å and *d*(Ga–Cl) = 2.168 Å (3.3). The smaller shift in the *T*<sub>2</sub> frequency reflects a competition between a similar positive change due to the force-constant hardening (+12 cm<sup>-1</sup> assuming the same dependence for *T*<sub>2</sub> than of the *A*<sub>1</sub> mode) and a negative change due to the increase in reduced mass (-8 cm<sup>-1</sup>), in good agreement with the final shift.

The temperature dependence of the Raman spectrum is similar for both compounds. The *A*<sub>1</sub> mode shifts to lower frequencies and the peak width broadens with increasing temperature. The frequency decreases with temperature at a rate of -0.034 cm<sup>-1</sup> K<sup>-1</sup> yielding a thermal coefficient 1/ν(∂ν/∂*T*) for the *A*<sub>1</sub> mode of -1.01 × 10<sup>-4</sup> K<sup>-1</sup>. This coefficient is similar to the bulk expansivity coefficients determined by X-ray diffraction in TCF [1.9 (2) × 10<sup>-4</sup> K<sup>-1</sup>] providing quantitative agreement between vibrational (Raman) and crystal structure (X-ray diffraction) thermal dependences.

### 3.3. Crystal structures and analysis

Phase transitions in TCF and TCG are characterized by reorientations of the constituent [NMe<sub>4</sub>]<sup>+</sup> and [MCl<sub>4</sub>]<sup>-</sup> ions, and can be visualized in terms of alignment of ‘chains’ formed by both ions along the unit-cell axis directions. The highest-temperature cubic phase, *cP22*, is a plastic crystalline phase and is the exception, with both ions rotationally disordered. Crystal and refinement data for TCF and TCG are given in Tables 3 and 4, relevant twin laws, scale factors and basis transformations are given in Table 5.

**Table 4**  
Crystallographic information for TCG phase sequence.

Chemical formula for TCF is  $C_4H_{12}N \cdot GaCl_4$ ,  $M_r = 285.68$ . Mo  $K\alpha$  radiation

	TCG- <i>oP88</i>	TCG- <i>mP22</i>	TCG- <i>cP22</i>
<b>Crystal data</b>			
Crystal system, space group	Orthorhombic, <i>Pbcm</i> ( <i>bca</i> ) (No. 57)	Monoclinic, <i>Pm</i> (No. 6)	Cubic, <i>Pm<math>\bar{3}m</math></i> (No. 221)
Temperature (K)	226	300	393
<i>a</i> , <i>b</i> , <i>c</i> (Å)	12.8329 (7), 14.1248 (4), 6.3718 (3)	6.4571 (5), 7.1456 (5), 6.4596 (6)	6.8504 (4), 6.8504 (4), 6.8504 (4)
$\beta$ (°)	90	91.721 (8)	90
<i>V</i> (Å <sup>3</sup> )	1154.97 (9)	297.91 (4)	321.48 (6)
Twin obliquity (°)	0.0	0.024	0.0
<i>Z</i>	4	1	1
<i>D<sub>x</sub></i> (Mg m <sup>-3</sup> )	1.643	1.525	1.476
<i>F</i> (000)	568	130	130
$\mu$ (mm <sup>-1</sup> )	3.250	3.148	2.917
Crystal size (mm)	0.10 × 0.12 × 0.20	0.10 × 0.12 × 0.20	0.05 × 0.10 × 0.12
<b>Data collection</b>			
Absorption correction	Multi-scan <i>CrysAlis</i>	Multi-scan <i>CrysAlis</i>	Multi-scan <i>CrysAlis</i>
<i>T<sub>min</sub></i> , <i>T<sub>max</sub></i>	0.53, 0.72	0.59, 0.73	0.57, 0.86
$\theta_{min}$ , $\theta_{max}$ (°)	3.2, 24.8	5.4, 26.3	3.0, 15.6
No. of measured, independent and observed [ <i>I</i> > 2σ( <i>I</i> )] reflections	14 843, 1032, 994	1254, 1254, 1231	1506, 30, 29
Unmerged total reflections	18 384	4705	6712
<i>R<sub>int</sub></i>	0.044	0.033	0.069
Range of <i>h</i> , <i>k</i> , <i>l</i>	<i>h</i> = 0 → 14, <i>k</i> = 0 → 16, <i>l</i> = 0 → 7	<i>h</i> = -7 → 8, <i>k</i> = 0 → 8, <i>l</i> = -8 → 8	<i>h</i> = 0 → 3, <i>k</i> = 0 → 3, <i>l</i> = 1 → 5
Range of unmerged <i>h</i> , <i>k</i> , <i>l</i>	<i>h</i> = -15 → 17, <i>k</i> = -17 → 18, <i>l</i> = -8 → 8	<i>h</i> = -8 → 8, <i>k</i> = -8 → 9, <i>l</i> = -8 → 8	<i>h</i> = 9 → 10, <i>k</i> = -10 → 10, <i>l</i> = -10 → 10
<b>Refinement</b>			
<i>R</i> [ <i>F</i> <sup>2</sup> > 2σ( <i>F</i> <sup>2</sup> )], <i>wR</i> 2, <i>S</i>	0.0464, 0.0941, 1.00	0.0425, 0.0995, 0.98	0.0951, 0.1549, 1.00
No. of reflections	1028	1254	29
No. of parameters	51	56	14
$\Delta\rho_{max}$ , $\Delta\rho_{min}$ (e Å <sup>-3</sup> )	1.13, -0.64	0.77, -0.44	0.48, -0.36

**Table 5**  
Summary of TCF and TCG phases and unit-cell dimensions from single-crystal diffraction data.

Phase	Space-group symmetry (standard setting)	<i>T</i> (K)	<i>a</i> (Å)	<i>b</i> (Å)	<i>c</i> (Å)	$\beta$ (°)	<i>V</i> (Å <sup>3</sup> )	Twin laws (scale factor)	Basis transformation
TCF- <i>oP88</i>	<i>Pbma</i> ( <i>Pbcm bca</i> )	220	13.1442 (8)	13.9946 (8)	6.4272 (3)	90	1182.27 (11)	–	–
TCF- <i>oP44</i>	<i>Pbm2</i> ( <i>Pma2 acb</i> )	295	6.4471 (5)	14.2753 (11)	6.4526 (5)	90	593.86 (8)	–	<i>a</i> /2, <i>b</i> , <i>c</i>
TCF- <i>mP22</i>	<i>Pm</i>	318	6.425 (3)	7.1480 (16)	6.4274 (18)	91.21 (3)	295.10 (16)	4 <sub>{010}</sub> : 0.358 (13), 2 <sub>{100}</sub> : 0.155 (11) 2 <sub>{101}</sub> : 0.094 (4)	<i>a</i> , <i>b</i> /2, <i>c</i>
TCF- <i>mP44</i>	<i>P2<sub>1</sub>/m</i>	365	6.574 (3)	14.156 (7)	6.594 (3)	93.86 (4)	612.26 (10)	4 <sub>{010}</sub> : 0.496 (18)*	<i>a</i> , 2 <i>b</i> , <i>c</i>
TCF- <i>cP22</i>	<i>Pm<math>\bar{3}m</math></i>	385	6.8470 (5)	6.8470 (5)	6.8470 (5)	90	321.00 (7)	–	–
TCG- <i>oP88</i>	<i>Pbma</i> ( <i>Pbcm bca</i> )	226	12.8329 (7)	14.1248 (4)	6.3718 (3)	90	1154.97 (9)	4 <sub>{010}</sub> : < 1%	–
TCG- <i>mP22</i>	<i>Pm</i>	300	6.4478 (14)	7.1316 (7)	6.4451 (8)	91.399 (14)	296.28 (8)	4 <sub>{010}</sub> : 0.463 (7)	<i>a</i> /2, <i>b</i> /2, <i>c</i>
TCG- <i>cP22</i>	<i>Pm<math>\bar{3}m</math></i>	393	6.8504 (4)	6.8504 (4)	6.8504 (4)	90	321.48 (3)	–	–

Consistent with the Raman measurements, both component ions are tetrahedral; at 226 K N–C bond lengths range from 1.468 (8) to 1.489 (8) Å with an average C–N–C angle of 109.65 (45)°, Ga–Cl bond lengths range from 2.167 (2) to 2.1701 (19) Å with average Cl–Ga–Cl angle of 109.86 (7)°. At 220 K, Fe–Cl bond lengths range from 2.1821 (9) to 2.1931 (12) Å with an average Cl–Fe–Cl angle of 109.7 (4)°.

At temperatures below 288 K (TCF) and 286 K (TCG) both materials crystallize in the *oP88* phase, which has the space group *Pbma* with cell dimensions: (TCF at 220 K) *a* = 13.1442 (8), *b* = 13.9946 (8) and *c* = 6.4272 (3) Å, *Z* = 4. As illustrated in Fig. 3(a), the ions in this phase are aligned along the *c*-axis in ‘chains’ in which successive ions are in the same orientation. Neighbouring chains along **a** and **b** contain

$[MCl_4]^-$  anions oriented 'up' or 'down' along **c** as a result of the inversion symmetry.

The most significant structural difference between TCF-*oP88* and TCG-*oP88* relates to the magnitude of anionic off-sets in the *ac* plane. In TCF-*oP88*  $[FeCl_4]^-$  anions are aligned, with small off-sets [0.006 (1) Å] in the *ac* plane. The corresponding TCG-*oP88* structure is similar, except that the off-sets of  $[GaCl_4]^-$  anions in the *ac* plane are much larger [1.077 (2) Å] than in TCF-*oP88*, discussed in more detail below (§3.6 and Fig. S1 of the supporting information).

Upon heating through the *oP88* → *oP44* phase transition to 295 K, TCF adopts an orthorhombic cell, space-group symmetry *Pbm2*, with unit-cell dimensions  $a = 6.4471$  (5),  $b = 14.2753$  (11) and  $c = 6.4526$  (5) Å,  $Z = 2$ . This structure corresponds to the corrected room-temperature structure described by Wyrzykowski, Pattek-Janczyk *et al.* (2008). The loss of *a*-glide symmetry leads to a halving of the *a* axis relative to TCF-*oP88* with **c** becoming a polar axis. Neighbouring chains along **a** now have ions in the same orientation, with alternation occurring only for neighbouring chains along **b** [*cf.* top-right projections in Figs. 3(*a*) and 3(*b*)].

The structure of the TCF-*mP22* phase was determined at 318 K. Accompanying the transition from TCF-*oP44* is a marked drop in the data quality as a result of twinning. The existence of twinning *via* pseudo-tetragonal symmetry operations in TCF-*mP22* phases (and the corresponding phase in TCG) seems paradoxical because this operation is not part of the point group symmetry of the lower-temperature *oP88* or

*oP44* phases. The twin law is thus not 'inherited' from the symmetry or domain structure of the orthorhombic phases, and its provenance is unclear.

TCF-*mP22* structure has a primitive monoclinic cell with unit-cell dimensions:  $a = 6.425$  (3),  $b = 7.1480$  (16),  $c = 6.4274$  (18) Å,  $\beta = 91.21$  (3)°, and space-group symmetry *Pm*. This cell can be transformed to a pseudo-orthorhombic *C*-centred setting with dimensions  $a = 8.9739$  (19),  $b = 9.204$  (2) and  $c = 7.1747$  (12) Å. These parameters are similar to those reported for the highly disordered structure of tetramethylammonium tetrachlorothallate(III) reported by Lenck *et al.* (1991) [ $a = 7.525$  (3),  $b = 8.946$  (4),  $c = 9.132$  (4) Å] and it seems possible that the structure is actually monoclinic and twinned by pseudo-merohedry.

It is usually the case that symmetry increases through a sequence of phase transitions induced by heating, and it is noteworthy that the point-group symmetry decreases for both TCF and TCG upon heating in the sequence *mmm* → [*mm2*] → *m*. An increase in symmetry is however seen in the lattice translations. The phase transition from TCF-*oP44* to TCF-*mP22* leads to a halving of the *b*-axis length, so that with respect to TCF-*oP88*, in TCF-*mP22*  $a' \simeq a/2$ ,  $b' \simeq b/2$ ,  $c' \simeq c$  (where the primed axes refer to *oP22* and the unprimed to *oP88*, see Table 5). All cations and all anions are now in the same orientation, leading to the loss of all glide symmetry (Fig. 3*c*). Successive  $[FeCl_4]^-$  anions are fully eclipsed resulting in short Cl⋯Cl contacts along **b** [3.544 (6) Å; 2 × the van der Waals radius of Cl = 3.64 Å; Alvarez, 2013].

A similar TCG-*mP22* phase is observed above 286 K, at 300 K:  $a = 6.4478$  (14),  $b = 7.1316$  (7) and  $c = 6.4451$  (8) Å,  $\beta = 91.399$  (14)°.

Calorimetry measurements suggested TCF-*mP22* to be stable over a 30 K range before a third transition at 344 K formed the TCF-*mP44* phase; diffraction data on this phase were collected at 365 K. At this temperature the crystal quality had degraded still further and appeared to consist of at least four domains and smaller fragments with no significant diffracted intensity beyond 1.0 Å. Reflections were indexed on a primitive monoclinic cell,  $a = 6.574$  (3),  $b = 14.156$  (7),  $c = 6.594$  (3) Å,  $\beta = 93.86$  (4)° with space-group symmetry *P2<sub>1</sub>/m*.

Numerous partially occupied C atom sites were located about the central N atom of the  $[NMe_4]^+$  cation in an approximately spherical distribution. This shell of C atoms was modelled using a spherical shell of electron density equivalent to four methyl groups.

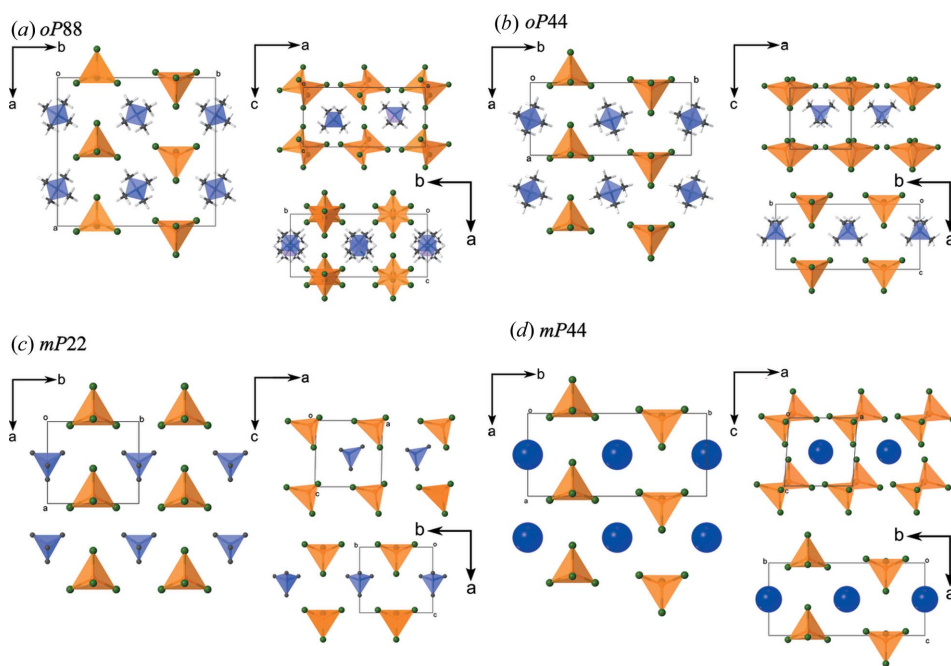


Figure 3

Projections of TCF structures illustrating the alternation of ion-chain alignment along each crystallographic axis. (*a*) TCF-*oP88* displaying alteration of ion-chain alignment in *b* and *c* directions. (*b*) In TCF-*oP44* the alteration of ion-chain alignment occurs in the *b* direction only. (*c*) After heating to the TCF-*mP22* phase all ion chains are aligned with only mirror symmetry present perpendicular to *b*. (*d*) In TCF-*mP44*, the arrangement of  $[FeCl_4]^-$  anions is similar to TCF-*oP44*, however, the  $[NMe_4]^+$  cations are rotationally disordered, increasing point symmetry of the cations during the transition from *mP22* to *mP44*.

Interionic distances increase as a result of the  $[\text{NMe}_4]^+$  motion and anionic rearrangement;  $\text{FeCl}_4-\text{FeCl}_4$  distances (given by the primitive unit-cell lengths) increase by 0.125 (4) Å relative to TCF-*mP22*, and 0.149 (5) and 0.139 (4) Å relative to the TCF-*oP44* structure. The increased average symmetry of the disordered  $[\text{NMe}_4]^+$  cations results in the loss of the *b* glide perpendicular to **a**.

In TCF-*mP44*,  $[\text{FeCl}_4]^-$  alignment alternates along the *b* axis only, with the ions fully aligned along **a** and **c**. The eclipsed configuration along **b** adopted in TCF-*mP22* is replaced by a fully staggered conformation, relieving the short, head-on  $\text{Cl}\cdots\text{Cl}$  contacts present in TCF-*mP22* [cf. bottom-right insets Figs. 3(c) and 3(d)].

### 3.4. Cubic plastic phase

Heating TCF through the final phase transition to 385 K produces the expected high-symmetry prototype phase (TCF-*cP22*), indexed with a primitive cubic cell with  $a = 6.8470$  (5) Å. The diffraction limit dropped to approximately 2 Å and highly structured diffuse scattering, taking the form of sheets in the {100} planes, could be observed, in addition to an inner diffuse ring as shown in Fig. 4(a). These features are characteristic of a plastic (or rotor) crystalline phase. Such phases exhibit rotational disorder of the constituent ions, often associated in ionic materials with sharp increases in dielectric constant such as those observed by Czaplá *et al.* (Czaplá *et al.*, 1985; Folmer *et al.*, 2008). Heating TCG through the phase transition to 393 K results in a similar significant drop in diffraction resolution to approximately 1.5 Å, also accompanied by sheets of diffuse scattering in the {100} planes. At 393 K, the TCG-*cP22* unit cell could be indexed to a slightly larger primitive cubic cell,  $a = 6.8504$  (4) Å.

Both structures were refined in  $Pm\bar{3}m$  with the tetramethylammonium cation occupying the body centre and

tetrachlorometallate at the origin. Both ions lie on Wyckoff positions with octahedral point symmetry  $m\bar{3}m$  ( $O_h$ ) which, in conjunction with the diffuse scattering, requires rotational disorder at both sites. One chlorine atom sits on the Wyckoff position  $24m$  at  $(x, x, z)$  with occupancy 0.125, the remaining Cl atom is on the higher symmetry  $8g$  position at  $(x, x, x)$  with an occupancy of 0.125. The off-axis position of the *m* chlorine produces a truncated dodecahedron representing eight orientations of the  $[\text{MCl}_4]^-$  anion.

The  $24m$  chlorine sites create short  $\text{Cl}\cdots\text{Cl}$  contacts of 2.52 (2) Å along the cell edges. For an Fe–Cl bond length of  $\sim 2.20$  Å and a chlorine van der Waals radius of 1.74 Å, the radius of a freely rotating  $[\text{FeCl}_4]^-$  anion would be  $\sim 3.94$  Å, requiring a primitive unit cell with  $a > 7.9$  Å, and a volume 1.5 times larger than the measured volume. As for the plastic crystal phase of  $\text{CBr}_4$  (another material with molecules of  $T_d$  symmetry occupying sites with  $O_h$  symmetry), the partial ordering of the  $[\text{FeCl}_4]^-$  anion site reflects the hindered nature of rotation at these sites requiring strong nearest-neighbour-correlated motion (Folmer *et al.*, 2008). Consistent with this, although the  $[\text{NMe}_4]^+$  cation was refined using a spherical shell of carbon density, a similar treatment for  $[\text{MCl}_4]^-$  yielded significantly worse fitting than the discrete disorder model. The final model is shown in Fig. 4(b).

### 3.5. Phase sequence analysis

Phase sequences for both TCF and TCG are similar with the exception of two additional intermediate phases TCF-*oP44* and TCF-*mP44*. Enthalpy changes derived from DSC data (Table 1) show that the transitions to intermediate phases in TCF require less energy than transitions in TCG. As a result, the total enthalpy changes for transition sequences  $Pbma \rightarrow [Pbm2] \rightarrow Pm$  and  $Pm \rightarrow [P2_1/m] \rightarrow Pm\bar{3}m$  are significantly lower for TCF. The DSC peaks corresponding to the transitions into and out of the *cP22* phases (*mP22* or *mP44*  $\rightarrow$  *cP22*) overlap; as a result, the enthalpy changes recorded by DSC are the sum for the two transitions. The 0.31  $\text{kJ mol}^{-1}$  difference between the TCG and TCF sequence reflects the fact that the  $[\text{NMe}_4]^+$  cations are already rotationally disordered in TCF-*mP44* before the onset of the *cP22* phase.

All phases of TCG and TCF can be considered as interpenetrating primitive cubic lattices in the CsCl-type, where each ion has eight neighbours. However, the reduced  $T_d$  point symmetry of each ion results in offsets from ideal positions, distorting each sublattice. For example, at the lowest temperature, the *oP88* phases show staggering in both cation and anion sublattices expressed in the alternating orien-

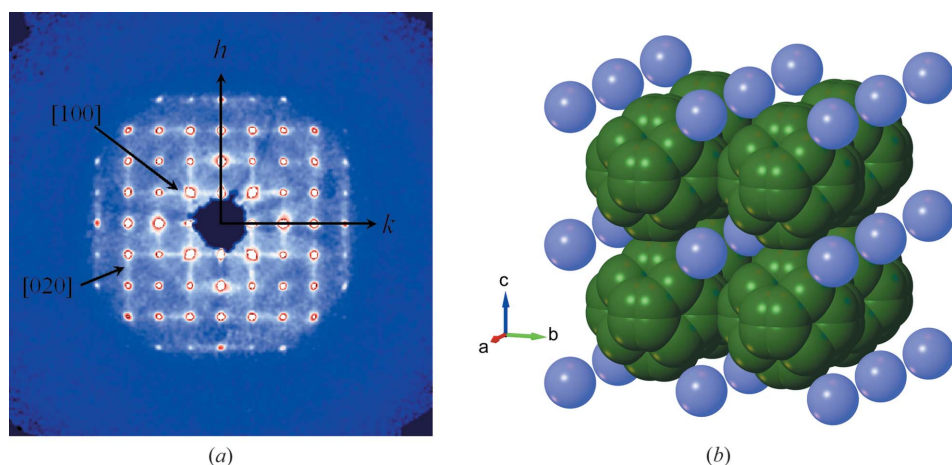


**Figure 4**  
TCF-*cP22*: (a) A simulated precession image of the  $hk0$  plane reconstructed from raw CCD data slices showing the sheets of diffuse scattering. (b) The spherical shape of the  $[\text{NMe}_4]^+$  cation (blue) is indicative of full rotational disorder on that site. The  $[\text{FeCl}_4]^-$  anion (green) however appears more constrained, occupying one of eight possible orientations. Short  $\text{Cl}\cdots\text{Cl}$  distances are present along each axis.

tations of the component ions. During each phase transition upon heating, translational symmetry is increased by the full occupation of just one orientation of the preceding staggered sublattice. The adoption of the highest symmetry  $Pm\bar{3}m$  structure is only achieved when the effective point symmetry of each component ion is  $O_h$  as in the  $cP22$  phases.

Mulliken population analysis (Mulliken, 1955) of  $[\text{GaCl}_4]^-$  and  $[\text{FeCl}_4]^-$  anions in optimized  $oP88$  structures shows a Cl-charge difference of  $0.22 e$  between  $[\text{GaCl}_4]^-$  ( $-0.56 e$ ) and  $[\text{FeCl}_4]^-$  ( $-0.78 e$ ) reflecting increased covalency in the  $[\text{GaCl}_4]^-$  anion. The difference results in closer Cl $\cdots$ Cl contacts in TCG- $oP88$  than in TCF- $oP88$ , the effect being largest in the Cl $\cdots$ Cl contacts along the  $a$  and  $b$  axes, which are shorter in TCG- $oP88$  by  $0.358$  (3) and  $0.119$  (2) Å, respectively. The short contacts are clearly visible in the fingerprint plots of  $[\text{MCl}_4]^-$  anions given in SI (Fig. S2 of the supporting information), and are consistent with the more linear  $M\text{---Cl}\cdots\text{Cl}$  contacts in TCG compared with TCF [ $142.59$  (8) versus  $116.99$  (4) $^\circ$ ], which is suggestive of a more

prominent Cl-based  $\sigma$ -hole in TCG. The difference is exaggerated further in the DFT-optimized structures of TCG- $oP88$  and TCF- $oP88$ , where  $\text{Ga}\text{---Cl}\cdots\text{Cl}$  is  $144.10^\circ$  and  $\text{Fe}\text{---Cl}\cdots\text{Cl}$  is  $114.79^\circ$ .

The differences between TCF and TCG were explored further using periodic DFT geometry optimizations of  $oP88$  models, both in the experimentally determined geometries and with Fe substituted for Ga and *vice versa*. It was found that the optimizations resulted in structures in which the initial anionic arrangements were preserved, that is, the TCF structure does not optimize into the experimentally observed TCG structure when Ga is substituted for Fe. The same is true when Fe is substituted for Ga in an optimization of the TCG structure. This feature of the energy landscapes of the two structures enables the energies of the different arrangements to be compared.

When Fe is substituted for Ga in the structure of TCG- $oP88$ , the final optimized configuration results in short Cl $\cdots$ Cl distances of  $3.5176$  Å along  $\mathbf{b}$ , significantly shorter

than in the arrangement in TCF- $oP88$ :  $3.8845$  Å ( $-0.3669$  Å,  $-9.45\%$ ). The total energy of this metal-substituted structure is  $9.12$  kJ mol $^{-1}$  higher than for a model of TCF obtained on optimizing the experimental TCF structure. Similarly for TCG, the optimized experimental configuration is significantly lower in energy than the Ga-substituted TCF- $oP88$  structure, the total energy difference between the two optimized geometries is  $6.73$  kJ mol $^{-1}$ .

### 3.6. Volume discontinuity and crystal packing

Volume-per-formula-unit ( $V/Z$ ) data for TCF and TCG derived from variable-temperature X-ray powder diffraction are shown in Fig. 5(a). The transition from TCF- $oP88$  to TCF- $oP44$  results in a significant reduction in  $V/Z$  of  $-4.1$  (4) Å $^3$  ( $-1.3\%$ ), an example of a discontinuous contraction through a phase transition. Similar data for TCG shows no such reduction in  $V/Z$ , with only a minor increase of  $+2.0$  (5) Å $^3$  (0.7%; Fig. 5).

Comparison of the reduced unit-cell dimensions for phases  $oP88$  and  $oP44$  (with  $a' = a/2$  and  $b' = b/2$  for  $oP88$ ,  $b' = b/2$  for  $oP44$  and  $mP44$ ) for TCF and TCG shows the  $V/Z$  decrease in TCF to be due to

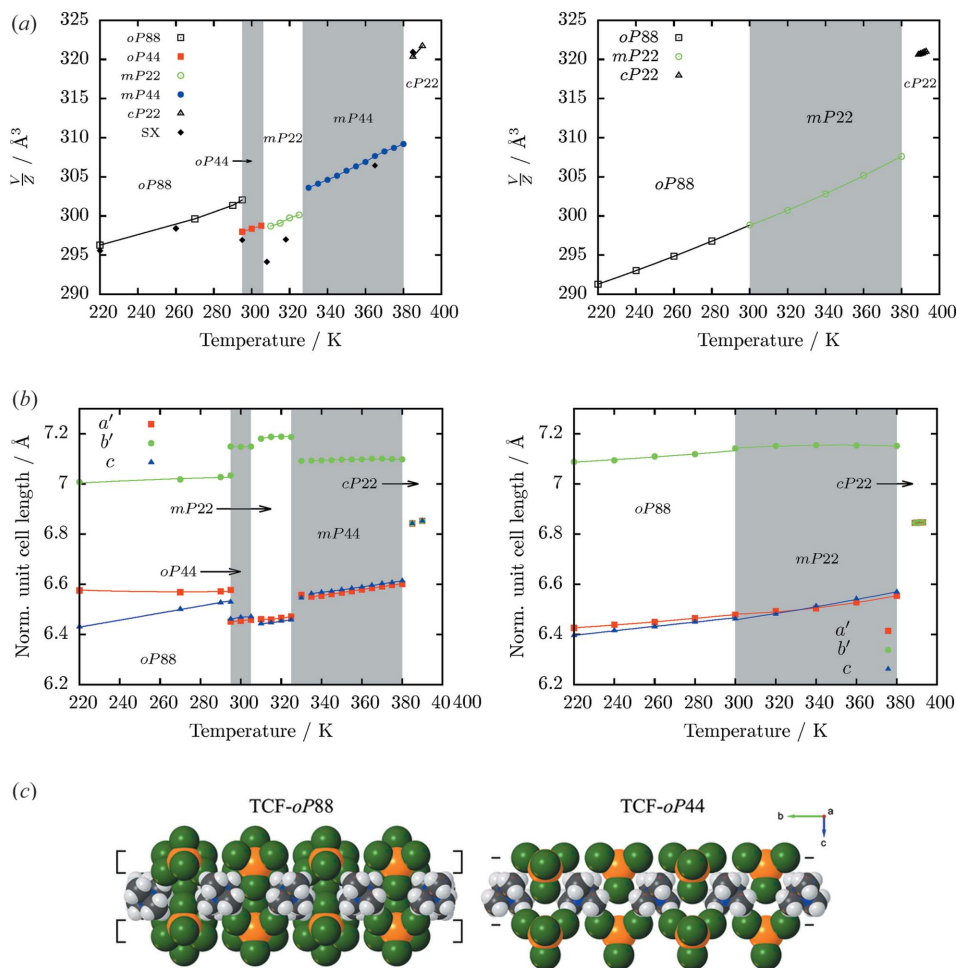


**Figure 5**

(a) Changes in volume per formula unit ( $V/Z$ ) with temperature for (left) TCF and (right) TCG as determined by variable-temperature X-ray powder diffraction and single-crystal data, labelled 'SX'. (b) Corresponding changes in normalized unit-cell dimensions with temperature. Lines correspond to thermal equation-of-state values. Errors bars are smaller than symbols. (c) Space-filling plots of TCF- $oP88$  and TCF- $oP44$ , the layers of Cl atoms, indicated with braces, pack more closely along  $c$  as a result of anionic reorientation.

contractions in the  $a'$  and  $c$  axes of  $-0.126$  (2) Å ( $-1.9\%$ ) and  $-0.068$  (3) Å ( $-1.0\%$ ) respectively, counter-acted by an increase along  $b'$  of  $0.115$  (4) Å ( $1.6\%$ ) as shown in Fig. 5(b).

The discontinuous changes in unit-cell lengths can be rationalized by examining the packing of  $[\text{FeCl}_4]^-$  anions. In both  $oP88$  and  $oP44$ ,  $[\text{FeCl}_4]^-$  ions are arranged to create buckled layers of Cl atoms in the  $bc$  plane composed of three of the four Cl atoms of each anion. The fourth Cl atom is projected above or below these planes along  $a$  (Fig. 5c, left). The degree of buckling within these layers determines how efficiently the planes can stack along  $a$ . On the transition from  $oP88$  to  $oP44$ , the buckling in these layers decreases from  $0.457$  to  $0.279$  Å; in effect the layers are 'flattened' accounting for the discontinuous reduction in  $a'$ .

The smaller reduction in  $c$  is due to both ions shifting from positions displaced above and below the  $c$ -glide in  $oP88$  to lie directly within the glide plane in  $oP44$ . At 220 K the displacements in  $[\text{NMe}_4]^+$  position are  $\pm 0.278$  (3) Å and remain unchanged up to at least 260 K [ $\pm 0.287$  (5) Å]. Similar, smaller displacements occur in the  $[\text{FeCl}_4]^-$  position; at 200 K anionic displacements are  $\pm 0.0740$  (3) Å increasing to  $\pm 0.1960$  (6) Å at 260 K, in TCF- $oP44$  these offsets are absent and ions lie directly in their respective planes.

The  $mP22 \rightarrow mP44$  transition is marked by a sharp volume increase of  $6.6$  (1) Å<sup>3</sup> accompanying the onset of rotational disorder in  $[\text{NMe}_4]^+$  cations. A similar increase of  $7.4$  (1) Å<sup>3</sup> occurs on the final transition to phase  $cP22$ , where the  $[\text{FeCl}_4]^-$  anions become rotationally disordered. This sequence is in marked contrast to TCG where during the  $mP22 \rightarrow cP22$  transition there is an increase of  $13.0$  (1) Å<sup>3</sup>, clearly due to the simultaneous onset of rotation in both ions.

#### 4. Conclusions

Through a combination of single-crystal and powder X-ray diffraction studies, differential scanning calorimetry, and optical transmittance, four new phases of tetramethylammonium tetrachloroferrate (TCF) between 120 and 385 K, and three phases of tetramethylammonium tetrachlorogallate (TCG) between 100 and 393 K have been identified. All three phases of TCG display an analogue in the phase sequence of TCF. Unusually, the point-group symmetry of both TCG and TCF decreases upon heating until high-temperature cubic plastic phases form, which are stable over a temperature range of just *ca* 2 K.

The presence of additional intermediate phases suggests greater conformational flexibility of the  $[\text{FeCl}_4]^-$  anion. The subtle, but energetically significant, structural differences in the low-temperature  $oP88$  phases result in the presence of shorter and more linear  $M-\text{Cl}\cdots\text{Cl}$  contacts in TCG, which are absent in TCF. Such close contacts are consistent with the presence of a prominent lone-pair- $\sigma$ -hole interaction in TCG. Calculations show the  $[\text{GaCl}_4]^-$  anion to be marginally more covalent than  $[\text{FeCl}_4]^-$ ; this subtle difference favours the formation of linear  $M-\text{Cl}\cdots\text{Cl}$  contacts in agreement with X-ray diffraction observations. Such interactions are highly directional and may act to reduce the conformational flex-

ibility of  $[\text{GaCl}_4]^-$ , explaining the absence of the intermediate phases. Comparison of the internal vibrational frequencies of  $[\text{MCl}_4]^-$  by Raman measurements supports this view.

These additional intermediate phases in TCF appear to allow a lower-energy pathway between phases than is possible in TCG. The structure of TCF- $mP44$  shows that the onset of rotational disorder of the constituent ions can occur at separate temperatures, in this case separated by 40 K. This structure is not adopted by TCG, and as a result both ions become disordered simultaneously upon the TCG- $mP22 \rightarrow$  TCG- $cP22$  transition at 393 K. This study shows that even subtle differences of electronic structure can have profound consequences for the crystal structures of even ionic compounds.

#### Acknowledgements

JB wishes to thank EPSRC and the Australian Government for funding.

#### Funding information

This work has been partially supported by MINECO under project No. MAT2015-69508-P.

#### References

- Agilent (2014). *ABSPACK, CrysAlisPro, SCALE*. Agilent Technologies, Yarnton, England.
- Alvarez, S. (2013). *Dalton Trans.* **42**, 8617–8636.
- Angel, R. J., Alvaro, M. & Gonzalez-Platas, J. (2014). *Z. Kristallogr. Cryst. Mater.* **229**, 405–419.
- Altomare, A., Casciarano, G., Giacovazzo, C. & Guagliardi, A. (1993). *J. Appl. Cryst.* **26**, 342–350.
- Barreda-Argüeso, J. A., Nataf, L., Rodríguez-Lazcano, Y., Aguado, F., González, J., Valiente, R., Rodríguez, F., Wilhelm, H. & Jephcoat, A. P. (2014). *Inorg. Chem.* **53**, 10708–10715.
- Berman, R. G. (1988). *J. Petrol.* **29**, 445–522.
- Betteridge, P. W., Carruthers, J. R., Cooper, R. I., Prout, K. & Watkin, D. J. (2003). *J. Appl. Cryst.* **36**, 1487.
- Clark, S. J., Segall, M. D., Pickard, C. J., Hasnip, P. J., Probert, M. I. J., Refson, K. & Payne, M. C. (2005). *Z. Kristallogr.* **220**, 567–570.
- Clay, R., Murray-Rust, J. & Murray-Rust, P. (1975). *Acta Cryst.* **B31**, 289–290.
- Czapla, Z., Czupiński, O., Galewski, Z., Sobczyk, L. & Waśkowska, A. (1985). *Solid State Commun.* **56**, 741–742.
- Flack, H. D. (1987). *Acta Cryst.* **A43**, 564–568.
- Folmer, J. C., Withers, R. L., Welberry, T. & Martin, J. D. (2008). *Phys. Rev. B*, **77**, 144205.
- Góśniowska, M., Ciunik, Z., Bator, G., Jakubas, R. & Baran, J. (2000). *J. Mol. Struct.* **555**, 243–255.
- Jakubas, R., Bator, G., Góśniowska, M., Ciunik, Z., Baran, J. & Lefebvre, J. (1997). *J. Phys. Chem. Solids*, **58**, 989–998.
- Kandhaswamy, M. A. & Srinivasan, V. (2002). *Bull. Mater. Sci.* **25**, 41–45.
- Kosturek, B., Podsiadla, D. & Czapla, Z. (1999). *Ferroelectrics*, **223**, 57–61.
- Lee, M. M., Teuscher, J., Miyasaka, T., Murakami, T. N. & Snaith, H. J. (2012). *Science*, **338**, 643–647.
- Lenck, M., Dou, S. Q. & Weiss, A. (1991). *Z. Naturforsch. A*, **46**, 777–784.
- López-Echarri, A., Ruiz-Larrea, I. & Tello, M. (1990). *J. Phys. Condens. Matter*, **2**, 513–523.

- López-Echarri, A., Tello, M. J., Socias, C. & Herreros, J. (1985). *J. Phys. C. Solid State Phys.* **18**, 2631–2642.
- Lutz, M., Huang, Y., Moret, M.-E. & Klein Gebbink, R. J. M. (2014). *Acta Cryst.* **C70**, 470–476.
- Mahoui, A., Lapasset, J., Moret, J. & Saint Grégoire, P. (1996). *Acta Cryst.* **C52**, 2671–2674.
- Melia, T. P. & Merrifield, R. (1971). *J. Chem. Soc. A*, pp. 1258–1261.
- Morosin, B. & Lingafelter, E. C. (1959). *Acta Cryst.* **12**, 611–612.
- Morosin, B. & Lingafelter, E. C. (1961). *J. Phys. Chem.* **65**, 50–51.
- Mulliken, R. S. (1955). *J. Chem. Phys.* **23**, 1833–1840.
- Nakamoto, K. (2006). *Handbook of Vibrational Spectroscopy*. New York: John Wiley and Sons, Ltd.
- Palatinus, L. & Chapuis, G. (2007). *J. Appl. Cryst.* **40**, 786–790.
- Perdew, J. P., Burke, K. & Ernzerhof, M. (1996). *Phys. Rev. Lett.* **77**, 3865–3868.
- Petříček, V., Dušek, M. & Palatinus, L. (2014). *Z. Kristallogr. Cryst. Mater.* **229**, 345–352.
- Ruiz-Larrea, I., Fraile-Rodríguez, A., Arnáiz, A. & López-Echarri, A. (2000). *J. Therm. Anal. Calorim.* **61**, 503–512.
- Ruiz-Larrea, I., López-Echarri, A. & Tello, M. J. (1987). *Solid State Commun.* **64**, 1099–1101.
- Sawada, S., Shiroishi, Y., Yamamoto, A., Takashige, M. & Matsuo, M. (1978). *J. Phys. Soc. Jpn.* **44**, 687–688.
- Schlessman, J. & Litvin, D. B. (1995). *Acta Cryst.* **A51**, 947–949.
- Schröder, L., Watkin, D. J., Cousson, A., Cooper, R. I. & Paulus, W. (2004). *J. Appl. Cryst.* **37**, 545–550.
- Sheldrick, G. M. (2015). *Acta Cryst.* **C71**, 3–8.
- Shimizu, H., Kokubo, N., Yasuda, N. & Fujimoto, S. (1980). *J. Phys. Soc. Jpn.* **49**, 223–229.
- Styczeń, E., Pattek-Janczyk, A., Gazda, M., Józwiak, W. K., Wyrzykowski, D. & Warnke, Z. (2008). *Thermochim. Acta*, **480**, 30–34.
- Tkatchenko, A. & Scheffler, M. (2009). *Phys. Rev. Lett.* **102**, 073005.
- Valiente, R. & Rodríguez, F. (1998). *J. Phys. Condens. Matter*, **10**, 9525–9534.
- Wolthuis, A. J., Huiskamp, W. J., de Jongh, L. J. & Carlin, R. L. (1986). *Phys. B+C*. **142**, 301–319.
- Wyrzykowski, D., Kruszyński, R., Kłak, J., Mroziński, J. & Warnke, Z. (2008). *Inorg. Chim. Acta*, **361**, 262–268.
- Wyrzykowski, D., Pattek-Janczyk, A., Maniecki, T., Zaremba, K. & Warnke, Z. (2008). *J. Therm. Anal. Calorim.* **91**, 279–284.
- Zubillaga, J., Lopez-Echarri, A. & Tello, M. J. (1988). *J. Phys. C. Solid State Phys.* **21**, 4417–4423.